Residual stress, microstructure, and structure of tungsten thin films deposited by magnetron sputtering

Y. G. Shen[a] and Y. W. Mai
Centre for Advanced Materials Technology (CAMT), Department of Mechanical and Mechatronic Engineering, University of Sydney, NSW 2006, Australia

Q. C. Zhang, D. R. McKenzie, and W. D. McFall
School of Physics, University of Sydney, NSW 2006, Australia

W. E. McBride
The Australian Key Centre for Microscopy and Microanalysis, University of Sydney, NSW 2006, Australia

(Received 20 April 1999; accepted for publication 22 September 1999)

The residual stress and structural properties of tungsten thin films prepared by magnetron sputtering as a function of sputtering-gas pressure are reported. The films were analyzed *in situ* by a cantilever beam technique, and *ex situ* by x-ray diffraction, cross-sectional transmission electron microscopy (TEM), x-ray photoelectron spectroscopy, electron energy-loss spectrometry, and energy-filtered electron diffraction. It is found that the residual stress, microstructure, and surface morphology are clearly correlated. The film stresses, determined in real time during the film formation, depend strongly on the argon pressure and change from highly compressive to highly tensile in a relatively narrow pressure range of 12–26 mTorr. For pressures exceeding ~60 mTorr, the stress in the film is nearly zero. It is also found that the nonequilibrium A15 W structure is responsible for the observed tensile stress, whereas the stable bcc W or a mixture of bcc W and A15 W are in compression. Cross-sectional TEM evidence indicates that the compressively stressed films contain a dense microstructure without any columns, while the films having tensile stress have a very columnar microstructure. High sputtering-gas pressure conditions yield dendritic-like film growth, resulting in complete relaxation of the residual tensile stresses. Structural details of the A15 W and amorphous W phases were also investigated at the atomic level using energy-filtered electron diffraction with reduced radial distribution function $G(r)$ analysis. By comparing the experimental and simulated $G(r)$ distributions, the A15 W structure is determined to be composed of ordered and stacking faulted W_3W structures and the amorphous W has a disordered structure of W_3O. The effect of oxygen in stabilizing the A15 phase found is explained on the basis of structural and thermodynamic stability. © *2000 American Institute of Physics.* [S0021-8979(00)00601-0]

I. INTRODUCTION

In recent years, there has been considerable interest in understanding the origin of residual stresses and microstructure in thin films. Many studies show that the mechanical, physical, and optical properties are strongly related to the film microstructure, which in turn is determined by the experimental conditions used in the deposition process. For the best-known examples, magnetron sputter-deposited refractory-metal films tend to have high residual stress, which undergoes a transition from compression to tension with increasing sputtering-gas pressure, resulting in dramatic differences in the film microstructure.

To date, metallic tungsten films have been prepared by different deposition techniques including: electron-beam evaporation,[1] chemical vapor deposition,[2–4] and dc or rf magnetron sputtering.[5–13] Interest in this system has been motivated by its useful properties, particularly in respect of its industrial applications, such as high electric conductivity, high melt temperature, high mechanical strength, good metal barrier performance, and fine patternability. In the case of sputter-deposited films, residual stress has been investigated and resultant crystallinity, density, electrical resistivity, and surface morphology of W films have been characterized as a function of processing conditions.[5–8] The effects of deposition temperature and postannealing on the phase transition of the W films have also been addressed.[9,10] However, correlation of residual stress with microstructure in the W films still has to be studied and clarified. Structural details of the nonequilibrium crystalline and noncrystalline phases in W films at the atomic level are substantially unknown and a subject of controversy due to large uncertainties involved in spectroscopic measurements and to different interpretations of experiments.[8–14] In particular, complications caused by the simultaneous presence of the forbidden reflections in the A15 W films observed in transmission electron diffraction (TED) have not been resolved yet.[7,15–17] In addition, the effect of oxygen impurities in stabilizing the A15 W structure is rarely systematically studied.

In this article the effects of the sputtering-gas pressure on the residual stress and structural properties in the W films, deposited by dc magnetron sputtering, are presented, in

[a]Electronic mail: yshen@mech.eng.usyd.edu.au

which some new features not reported in previous studies of this system have been revealed. The evolution of the film stress was characterized by *in situ* real time stress measurement. The phase and microstructure of the W films were analyzed by x-ray diffraction (XRD) and cross-sectional transmission electron microscopy (TEM). The oxygen content of the films was measured by x-ray photoelectron spectroscopy (XPS) and electron energy-loss spectrometry (EELS). Furthermore, details of the A15 W and amorphous W (*a*-W) structures formed at different sputtering-gas pressures were investigated at the atomic level for the first time using energy-filtered electron diffraction (EFED) with reduced radial distribution function $G(r)$ analysis. By comparing the experimentally determined and theoretically calculated $G(r)$ distributions, structural models for the A15 W and *a*-W phases are proposed. The role of oxygen impurities in stabilizing the A15 phase was also elucidated by *in situ* anneal in the TEM and EELS system.

II. EXPERIMENT

The tungsten films were deposited by dc planar magnetron sputtering using a 99.99% pure tungsten disk (50 mm in diameter) in a deposition chamber with a base pressure of 3×10^{-6} Torr. The substrates were conventionally cleaned, mounted on a substrate holder located 70 mm above the center of the target, and coated using a sputtering power density of 4 W/cm^2, and an argon gas at pressures varying from 2 to 100 mTorr. Prior to deposition, the target was sputter cleaned for 5 min while the substrates were isolated from the plasma by a shutter. The substrates were 330 μm thick silicon with dimensions 10×10 mm^2, cleaved from 76 mm wafers of *p*-type (100) silicon ($\rho\sim1$–10 Ω cm). The thicknesses of the tungsten films were determined by measuring the step height between masked and unmasked regions on the substrate using a stylus-type surface profilometer (Tencor P10).

The film stress measurements were performed using a cantilever beam technique[18] to detect changes in the substrate curvature. The film stress was then calculated using Stoney's equation[19]

$$\sigma=\frac{1}{6R}\frac{E}{(1-\nu)}\frac{D^2}{d}, \tag{1}$$

where E, ν, and D are the Young's modulus, Poisson's ratio, and thickness of the substrate, respectively [for Si(100), $E/(1-\nu)$ equals 181 GPa], d is the film thickness (assuming that $d\ll D$), and R is the radius of curvature of the substrate. It has been verified that the original curvature of a bare silicon wafer is negligible compared with the measured curvatures after deposition.

The XRD measurements were carried out using a Siemens D5000 diffractometer with a Cu tube operated at 40 kV and 30 mA and a diffracted-beam graphite monochromator. To ascertain the absolute values of the 2Θ diffraction angles, the diffractometer was calibrated with respect to the peak positions of a Si calibration standard.

The films were also analyzed by XPS using a Kratos Axis/800 hemispherical energy analyzer equipped with an unmonochromatized Mg $K\alpha$ x-ray source ($h\nu=1253.6$ eV). The binding energy scale was calibrated against Ag $3d_{5/2}$ at 368.25 eV and the instrumental energy resolution, measured using the same peak, was 0.9 eV (pass energy set at 20 eV). Charging corrections were made using the as-measured Fermi level of Ag and Au pieces on the metallic substrate holder using the Mg $K\alpha$ radiation as a reference.

EELS spectra and EFED patterns were acquired using a Phillips EM430 TEM fitted with a Gatan 666 parallel-detection EELS operating at 300 kV. The procedures for data collection of EFED patterns have been described previously.[20,21] Briefly, the electrons passed a postcolumn magnetic EELS to record the elastic distributions. The electron intensity was sequentially recorded under computer control as a function of the reciprocal space coordinate by shifting the diffraction pattern across the entrance aperture of the spectrometer. The background subtraction was performed using the tabulated electron scattering factors.[22]

Cross-sectional TEM images were obtained in a Phillips EM430 microscope operated at 300 kV. Specimens for cross-sectional TEM analysis were prepared by face-to-face gluing with epoxy resin, and mechanical thinning, followed by Ar^+ ion milling for the final thinning to obtain electron transparency. A range of samples were also floated off NaCl for EELS and EFED measurements.

III. RESULTS

A. *In situ* residual stress measurements

It is well known that the elastic behavior of tungsten is ideally isotropic. Therefore, the thin W films were expected to contain a biaxial state of stress which has rotational symmetry with respect to the surface normal. This was verified by measurement of the in-plane angle-dependent lattice strains in several different directions by XRD using the $\sin^2\Psi$ method[23] and was found to be the case within experimental uncertainty ($\pm10\%$). To follow the residual stress evolution during thin film deposition, a cantilever beam technique for *in situ* measurement of the stress was developed recently in our laboratory. The measurement reveals how the sputtering-gas pressure influences the formation of residual stresses in the W films. Figure 1 shows the pressure dependence of the instantaneous stress (force per unit width) as a function of film thickness. These four curves display a typical evolution which is frequently encountered when varying the processing conditions in dc and rf-powered sputtering techniques. The film deposited at a low pressure of 3.4 mTorr shows an increasing instantaneous compressive stress with film thickness. A remarkable evolution of the instantaneous stress with increasing film thickness was observed in the W films deposited at 12 mTorr. A state of tensile stress appears in the first stage of film growth, whereas the stress reversal is observed after a film thickness of about 50 nm was reached. The film prepared at an intermediate pressure of 26 mTorr exhibits tensile instantaneous stress. At high pressure, $\sim$60 mTorr, the film is almost free of residual stresses up to 200 nm.

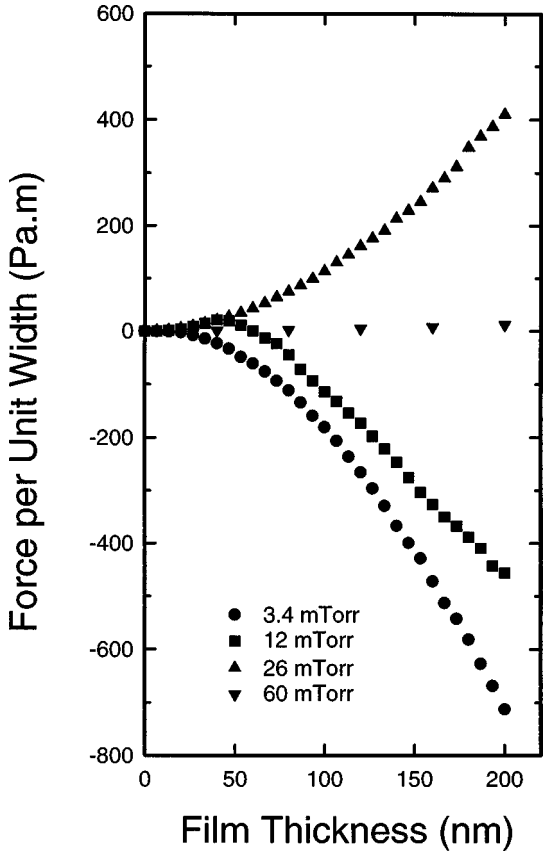

FIG. 1. Force per unit width vs film thickness for W films deposited at several different Ar pressures.

Figure 2 shows the evolution of the stress for a series of 150-nm-thick W films as a function of sputtering-gas pressure. In our study, the power density was fixed, and the only variable was the Ar pressure. No delamination of the films was observed in all cases. In the low pressure range of 2–12 mTorr, the W films are subjected to high compressive stresses. As the sputtering-gas pressure is increased, the stress changes from compression to tension, reaching a maximum, and with further increase the stress is gradually decreased. For pressures exceeding about 60 mTorr the stress in the film is nearly zero. This dependence of residual stress on sputtering-gas pressure shown in Fig. 2 has already been reported in many other refractory-metal films,[24–26] deposited by dc and rf magnetron sputtering.

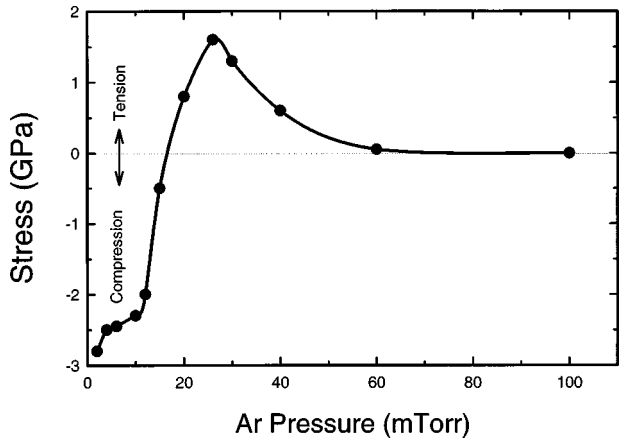

FIG. 2. Film stress in 150-nm-thick W films as a function of Ar sputtering-gas pressure.

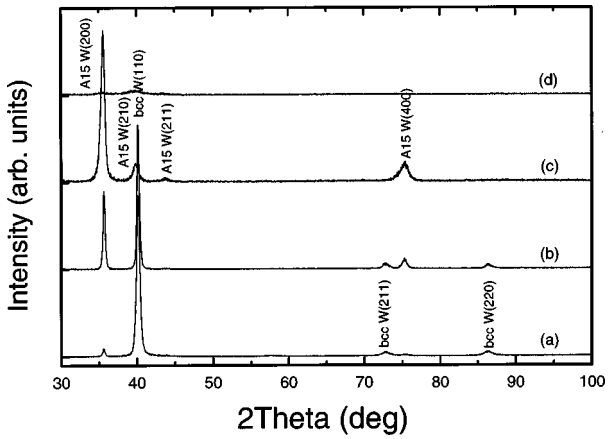

FIG. 3. XRD diffraction patterns showing the different structure in 150-nm-thick W films as a function of Ar sputtering-gas pressure at: (a) 3 mTorr, (b) 12 mTorr, (c) 26 mTorr, and (d) 60 mTorr.

The stress-versus-pressure curve was obtained after repeated deposition over many days. The results are reproducible. The compressive stress observed at low sputtering-gas pressures was attributed to the bombardment of sputtered tungsten atoms and reflected Ar neutrals through the atomic peening process.[24] Conversely, the absence of energetic particle bombardment at elevated pressures due to more scattering events in the sputtering-gas region leads to tensile stress. With further increasing sputtering pressure, a complete relaxation of residual stresses occurs.

B. X-ray diffraction

Our XRD measurements indicate that the sputtering-gas pressure strongly determines whether the film will have a stable bcc W phase, a metastable A15 W phase, or a mixture of the two, and even an amorphous W phase. Typical XRD Θ–2Θ scans in the Bragg–Brentano geometry show the structural changes in the 150-nm-thick W films as a function of sputtering-gas pressure (Fig. 3). At a pressure of 3 mTorr [Fig. 3(a)], the (110), (211), and (220) reflection peaks of bcc W are mainly observed, while the film deposited at 12 mTorr [Fig. 3(b)], shows a mixture of the bcc W and A15 W phases. At 26 mTorr [Fig. 3(c)], only pure A15 W phase reflections [(200), (210), (211), and (400) peaks] are observed. On further increasing pressure up to 60 mTorr [Fig. 3(d)], no structure feature is seen, indicating that an amorphous phase was developed. The lattice parameters of the crystal structures from several XRD patterns were calculated to be 0.3168 nm for bcc W and 0.5046 nm for A15 W, in good agreement with the reported bulk values of 0.3165 and 0.504 nm, respectively.[27] From the XRD scans, we also note that all films predominantly containing the bcc phase showed a strong $\langle 110 \rangle$ preferred orientation.

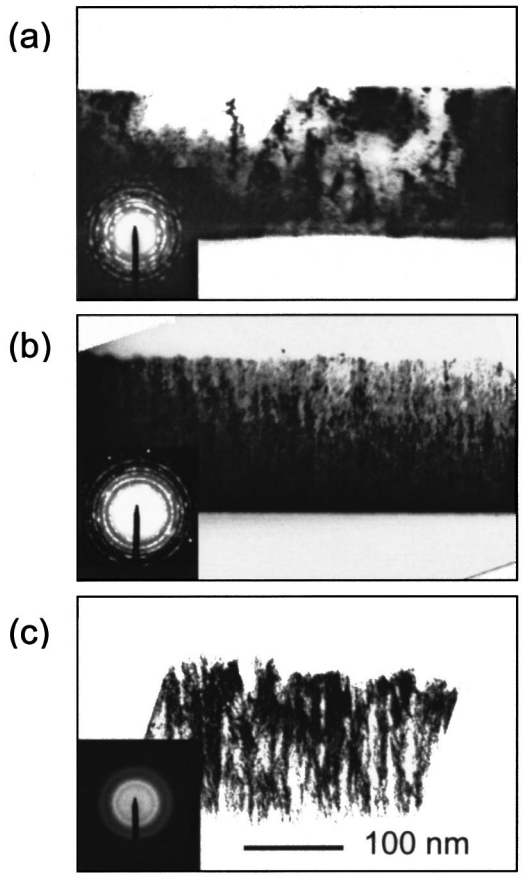

FIG. 4. Cross-sectional TEM images showing the microstructure evolution of 150-nm-thick W films as a function of Ar sputtering-gas pressure (the corresponding XRD diffraction patterns are given in Fig. 3). The electron diffraction patterns (insets) are also shown: (a) at 12 mTorr, (b) at 26 mTorr, and (c) at 60 mTorr.

C. Cross-sectional transmission electron microscopy

The evolution of the microstructure of the W films with sputtering-gas pressure has been investigated by examining the cross sections in comparable thickness films by means of cross-sectional TEM. Figure 4 shows bright-field cross-sectional TEM micrographs and corresponding selected-area electron diffractions of 150-nm-thick W films. It was found that the films deposited at a low pressure of 12 mTorr (compressive stress, Fig. 2) contain a dense microstructure without any columns shown in Fig. 4(a). No evidence of the presence of voids in compressive stress films was observed. Most of the microstructure is composed of large bcc W grains with a few fine A15 W grains. The coarse bcc grains are also evident from the spotty rings shown in the inset of Fig. 4(a). For a film deposited at 26 mTorr (maximum tensile stress), a very columnar microstructure is observed [Fig. 4(b)]. It is interesting to note that the surface structure in Fig. 4(b) has changed compared to that in Fig. 4(a), each column having a domed top. An in-plane field-emission scanning electron microscopy (JEOL JSM-6000F) image of an as-deposited 150-nm-thick film also shows that the isolated voids exist at the column boundaries, revealing that the columns are not free standing (not shown). At a high pressure of ~60 mTorr, where the stress is nearly zero, the columnar microstructure has disappeared and a dendritic-like structure is observed [Fig. 4(c)]. Compared to the tensile stress film in Fig. 4(b), the amount of column boundary voids and the extent of surface roughness are more dramatic. The electron diffraction pattern obtained from the zero stress film shows an amorphous feature. This is in good agreement with the XRD measurements described previously. These results clearly show that the residual stress level in the films is strongly correlated to their microstructure.

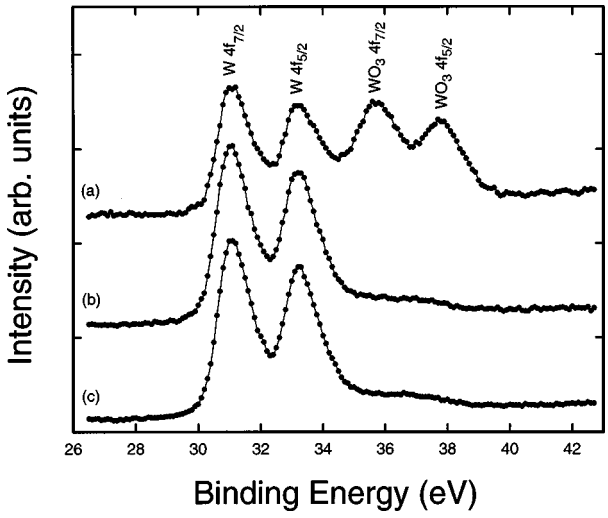

FIG. 5. Typical W $4f$ XPS spectra for: (a) the as-deposited 150-nm-thick A15 W sample, (b) the same sample at a depth of approximately 8 nm; and (c) the 150-nm-thick bcc W sample at a depth of approximately 8 nm. The films are those used for Figs. 3(b) and 3(c), respectively.

D. X-ray photoelectron spectroscopy

It was previously shown that the A15 structure was most probably induced by oxygen impurities incorporated in the films during growth.[8–13] However, no consensus has yet been reached whether the A15 film contains a stoichiometric tungsten suboxide W_3O or a metastable form of tungsten in which a small amount of oxygen is present. In addition, the oxygen dependence on the bcc W, A15 W, and *a*-W phases is rarely systematically studied. Both XPS and EELS (see below) measurements are well suited for elucidating this effect.

We have performed an XPS analysis of the bcc W, A15 W, and *a*-W films. Although the wafer was conventionally cleaned before deposition, it was exposed to air prior to the XPS measurement (as were all of the samples) and therefore contains surface oxide contamination. Overview spectra from these films revealed, in addition to the dominant W and O related peaks, a very small C $1s$ peak was also present and disappeared after the sample was irradiated with a small Ar ion dose. Figure 5 shows typical high resolution XPS spectra in the W $4f$ energy region obtained from the A15 W and bcc W films. In Fig. 5(a), the typical as-deposited A15 W film exhibits four characteristic peaks at 31.2, 33.3, 35.6, and 37.7 eV, among which the first two peaks represent W $4f_{7/2}$ and W $4f_{5/2}$ electrons for elemental tungsten (zero oxidation state) and the latter two peaks at higher binding energies correspond to those for a tungsten oxide. After a few minutes

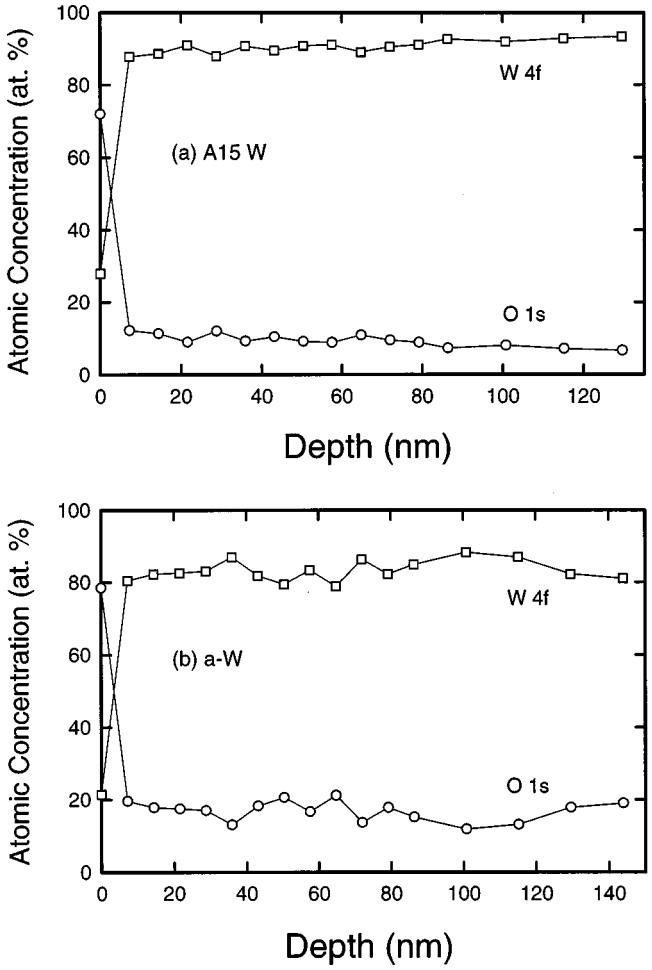

FIG. 6. XPS depth profiles of: (a) the A15 W and (b) the *a*-W samples. Films are those used for Figs. 3(c) and 3(d), respectively.

Ar sputter cleaning to remove the contamination layer, the XPS spectrum [Fig. 5(b)] from the same A15 W film as Fig. 5(a) indicates that the A15 W is a metallic phase with binding energies identical to bcc W [Fig. 5(c)].

Tungsten and oxygen depth profiles for the A15 W and *a*-W samples are shown in Figs. 6(a) and 6(b), respectively. As expected, both film surfaces contain a considerable amount of oxygen due to surface oxide contamination. Below this surface layer, however, the oxygen concentration becomes essentially constant at a value of about 10 at. % for the A15 W sample and 18 at. % for the *a*-W sample. When a similar measurement was carried out on a bcc W sample (not shown), the oxygen concentration was reduced to be about 1 at. %.

On a day-to-day basis, the bcc W, A15 W, and *a*-W films deposited under different sputtering-gas pressures were readily produced and very reproducible in such a way that the bcc W is a stable phase with little oxygen contamination (typically <2 at. % oxygen), the A15 W is a metastable form of tungsten in which a small amount of oxygen is present, whereas the *a*-W contains more oxygen (close to the 25 at. % oxygen necessary for a disordered W_3O stoichiometry). Detailed chemical composition analysis on six freshly repeated depositions at a pressure range of 20–30 mTorr in the XPS system indicates that the A15 W films prepared under the experimental conditions contained ~5–12 at. % oxygen in the film thickness range of 50–200 nm. Our measurements unambiguously show that the A15 W structure is stabilized by oxygen impurities without forming a W_3O compound. This conclusion has been further confirmed below by using EELS measurements.

Close examination of the deposition processing reveals that the most likely source of oxygen contamination was either from residual oxygen in the deposition chamber or from the tungsten sputter target under the present experimental conditions. The difference in oxygen concentration was mainly controlled by the deposition rate, i.e., the competitive effect between the tungsten deposition rate and the contamination incorporation rate. The longer the sputtering time, the lower the oxygen content in the film.

E. Electron energy-loss spectrometry

A series of O *K*-edge EELS spectra are shown in Fig. 7 for three 100-nm-thick W films prepared at different Ar sputtering pressures. The energy of the O *K*-edge peak was calibrated using C $1s-\pi$ transition peaking at 284.0 eV, which is due to carbon absorbed on the specimen by the electron beam. It is noted that the O *K*-edge loss spectra observed are remarkably similar, indicating that the matrix element and the density of states accessible to an O *K*-shell electron are identical for the three films investigated. The O *K*-edge peak observed at around 532 eV in Fig. 7 can be identified to be the transition from O $1s$ to W $5d$. We also note that the signal in the O K-edge loss spectra is different for each film, mainly due to the different oxygen concentration contained in the films. The analysis of EELS spectra to yield quantitative concentration is straightforward. The O K-edge is superimposed upon a monotonically decreasing background. The background is modeled by a least-square fit of a power-law energy dependence over an energy region immediately preceding the *K* edge and a subsequent extrapolation to higher energies. After background subtraction, the O *K*-edge intensities are integrated over an energy window (~50 eV). The values for O *K*-edge intensities are proportional to the elemental concentration. Quantification was done using a stoichiometric crystalline sample of $W_{0.75}O_{0.25}$ as a standard.[28] The results derived from these films indicate that the O impurities in the bcc W, A15 W, and *a*-W films are 2%±2%, 15%±2%, and 22%±3%, respectively. The quoted errors reflect the magnitude of random scatter based on 4–6 independent measurements.

Further extensive measurements of oxygen impurities incorporated in the films using EELS analysis have been carried out on a series of samples: three bcc W, five A15 W, and five *a*-W in the film thickness range of 50–100 nm. The results indicate that the as-deposited bcc W, A15 W, and *a*-W films contained 1–4, 6–15 and 18–26 at. % oxygen, respectively. These values are in good agreement with the XPS results, described above.

The A15 W crystal structure is metastable because it transforms to the stable bcc W by anneal. However, in many cases many researchers have misinterpreted the origin of this transformation as a stress effect or a critical thickness in-

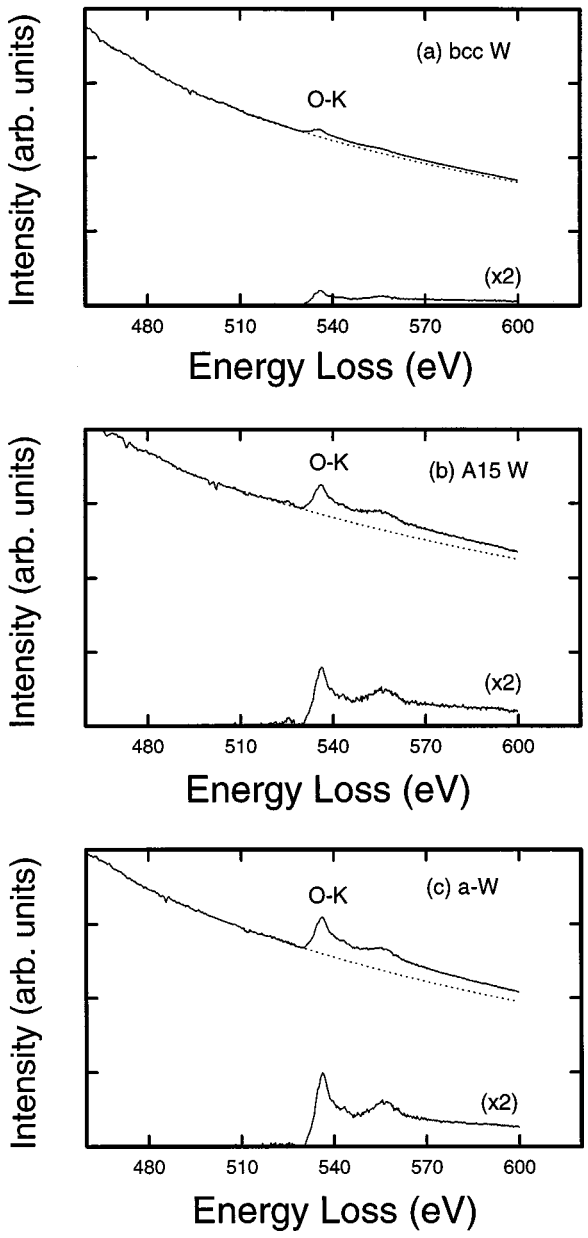

FIG. 7. Oxygen *K*-edge EELS spectra obtained from three 100-nm-thick films: (a) bcc W, (b) A15 W, and (c) *a*-W. Fitted background and spectra with the background subtracted are also shown for each case.

duced transformation. To understand the role of oxygen in forming and stabilizing the A15 W structure, three independent measurements were carried out using EELS, TED, and XRD analysis. The EELS results are shown in Fig. 8, in which the oxygen concentrations of a 50-nm-thick film derived from the O *K*-edge EELS spectra are plotted as a function of film temperature. The points labeled A and B gave the O *K*-edge spectra shown. The corresponding XRD patterns (also labeled A and B) recorded from the original A15 W film (the 50-nm-thick film was deposited on a Si substrate simultaneously) and after transforming to the bcc are also shown. The results indicate that with increasing temperature the oxygen atoms move increasingly outward. The A15 W phase is completely transformed to the bcc W structure by annealing to 625 °C. The most interesting feature for this

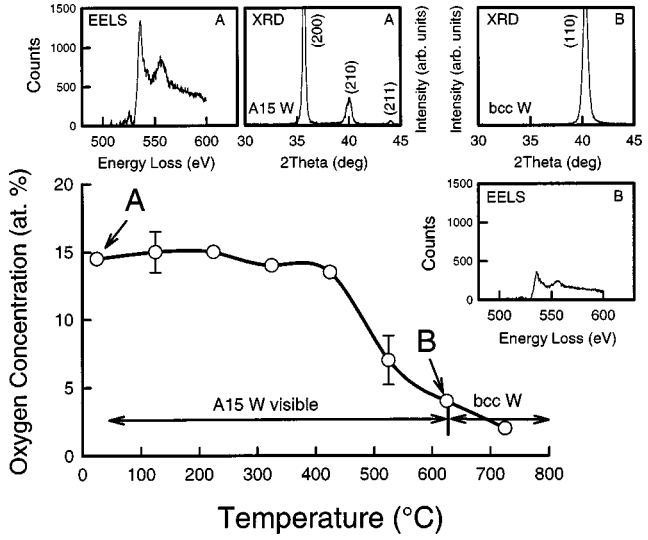

FIG. 8. The oxygen concentration as a function of film temperature by EELS. Error bars are based on 4–6 measurements. From each point, data were taken during *in situ* heating at 20 °C min^{-1}, held for 5 min, and then the O *K*-edge spectrum was taken. The EELS spectra and corresponding XRD patterns labeled A and B recorded from the original and after the phase transformation are also shown.

observation is that the phase transformation from A15 to bcc by higher temperature annealing was accompanied by reduction of oxygen in the films. These results have not been previously published and further support the role of oxygen in forming and stabilizing the A15 W structure. This direct evidence leads one to believe that the A15 phase is stabilized by a small amount of oxygen in the film without forming a W_3O compound. We can suggest that the transformation from A15 W to bcc W is thermally activated requiring higher temperature to cause the oxygen impurities to outdiffuse (segregate to the surface) and to bring about the long-range ordering, and then to transit to the stable bcc structure. We would also like to point out that, once a bcc W phase was prepared, the reverse transformation has never been observed.

F. Energy-filtered electron diffraction

EFED is a good technique to extend the structural study of polycrystalline and amorphous films not accessible in most other techniques. In order to address the structural question related to atomic arrangement for the A15 W and *a*-W films, the EFED technique together with the reduced radial distribution function $G(r)$ analysis are applied in the present study. $G(r)$ is defined by

$$G(r)=4\pi r[\rho(r)-\rho_0], \tag{2}$$

where ρ_0 is the average atomic number density, and $\rho(r)$ is the atomic density at a distance r from a given atom at the origin. $G(r)$ is obtained by collecting EFED patterns $I(q)$ using Fourier sine transformation in real space:

$$G(r)=8\pi\int_0^{q_{\max}}\frac{I(q)-Nf^2}{Nf^2}qD(q)\sin 2\pi rq\,dq, \tag{3}$$

where $q=2\sin\Theta/\lambda$, 2Θ is the scattering angle, λ is the de Broglie wavelength of the electrons, N is the number of atoms in the sample, f is the atomic scattering factor, and $D(q)$ is a damping function, in this case $D(q)=\sin(\pi q/q_{\max})/(\pi q/q_{\max})$. The data were collected to a maximum value of q, $q_{\max}$, of at least 3.0 Å^{-1}.

The theoretical $G(r)$ were calculated from the diffraction intensities $I(q)$ determined using the Debye scattering equation

$$I(q)=\sum_{m=1}^{N}\sum_{n=1}^{N} f_m f_n \frac{\sin 2\pi q r_{mn}}{2\pi q r_{mn}} \tag{4}$$

for an array of N atoms which takes all orientations in space and r_{mn} is the distance between atoms m and n. The $I(q)$ was computed for the same range of q and processed in the same manner as the experimental data, then Fourier sine transformed to produce the experimental $G(r)$.

Figure 9 shows the EFED patterns in the momentum space obtained from the films investigated. The diffraction pattern was calibrated by indexing the diffraction pattern of a known standard of polycrystalline aluminum [see Fig. 9(a)]. The $I(q)$ from the A15 W film prepared at an Ar sputtering pressure of 26 mTorr shows the polycrystalline long-range order features [Fig. 9(b)]. The characteristics of the patterns agree with observations obtained by TEM. All the lines (hkl) corresponding to the A15 phase are clearly detected. It is interesting to note that some forbidden reflection peaks, such as (100) at $q\approx 0.20\,\text{Å}^{-1}$ and (110) at $q\approx 0.28\,\text{Å}^{-1}$, appear in the $I(q)$ curve, indicating the existence of ordered substitutional or interstitional lattice defects in the A15 W structure. These observations are in good agreement with previous studies by several research groups using TED.[7,15–17] These authors, however, discuss only the stacking faults formed in the A15 W films without further justification. In contrast, the pattern from the *a*-W film prepared at a high pressure of ~60 mTorr exhibits characteristics typical of the amorphous state [Fig. 9(c)]. We observe three broad and diffused halos without contamination of the Bragg peaks since the TEMs in the dark field do not reveal microcrystallites. The observed feature in $I(q)$ is a strong intensity at $q=0.42\,\text{Å}^{-1}$. We also note that the diffraction intensity pattern exhibits a split second peak, which is a form of behavior found for many amorphous metal or metal–metalloid alloys, and is in agreement with the dense random packing of the hard spheres model.

In order to obtain detailed structural information, the most effective and direct method is to compare the experimentally determined $G(r)$ with the corresponding theoretically calculated curve because a relationship in the coordinate space can be interpreted much easier than the correlation in the momentum space. $G(r)$ is related to the probability of finding an atom in a shell of thickness dr at a distance r from an arbitrary origin. Successive peaks in $G(r)$ correspond to first-, second-, and higher-order neighbor atomic distributions. The theoretical $G(r)$ for the model structure was calculated by appropriate $q-r$ Fourier sine transformation using Eq. (4).

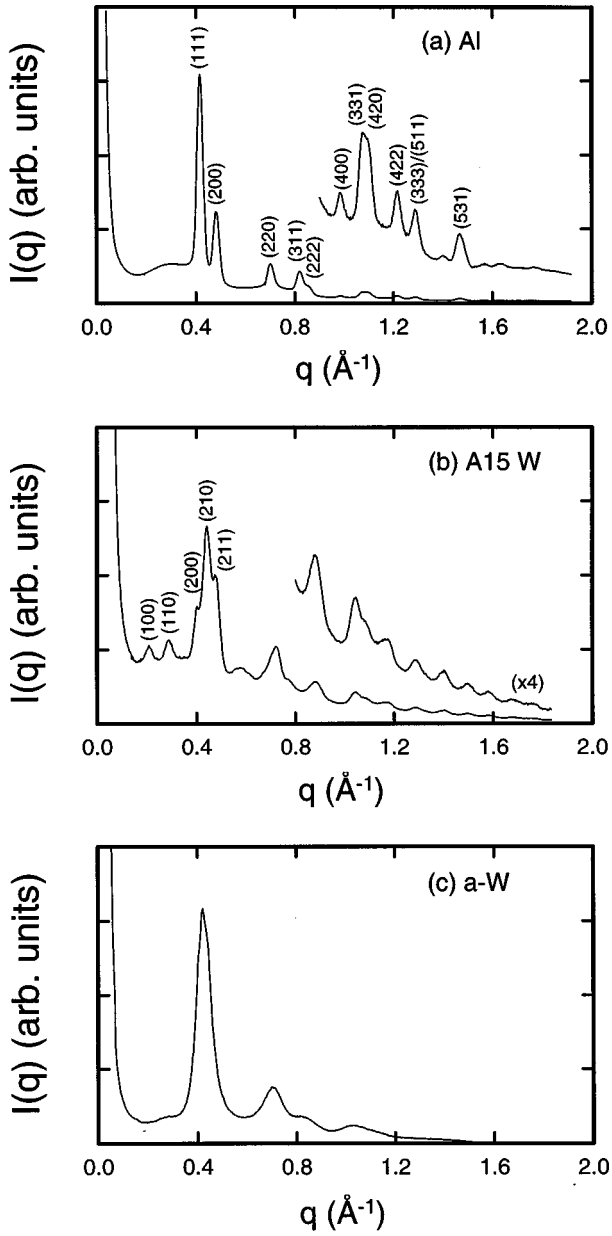

FIG. 9. Experimentally measured EFED intensities $I(q)$ as a function of q for three 50-nm-thick films; (a) the polycrystalline Al film for Miller index calibration, (b) the A15 W film deposited at 26 mTorr, and (c) the *a*-W film deposited at 60 mTorr.

A major question concerning A15 W is whether it is an ordered W_3W phase or a stacking faulted W_3W structure or a mixture of both. There are two different atomic positions in the A15 (A_3B) structure,[29] six A positions with two nearest neighbors at a distance of 2.52 Å and two B positions with 12 nearest neighbors at a distance of 2.82 Å. The initial stacking sequence for A15 is ABCBABCB (layers A, B, C, and B are spaced by 1/4 *a*, the lattice parameter of the A15 structure). The observation of the forbidden reflections in an electron diffraction pattern restricts any structural models to the different stacking of A15 layers. We consider three possible stacking faulted sequences: ABBCABBC, ACBBACBB, and ABABABAB, respectively. It is noted that the ABABABAB stacking is a twin-related W_3W structure. Close examination reveals that the nearest neighbor W–W distance of 1.78 Å in both ABBCABBC and ACBBACBB stacking structures cannot be true because the

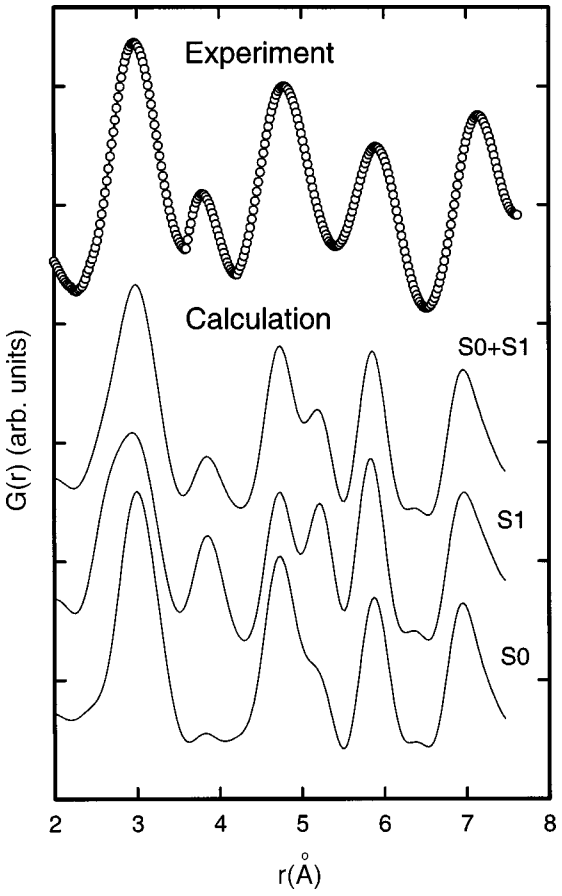

FIG. 10. Comparison of the theoretically calculated $G(r)$ for the A15 W structure using the models of S0, S1, and mixed (S0+S1) with the experimentally determined data. Some curves have been displaced vertically for clarity.

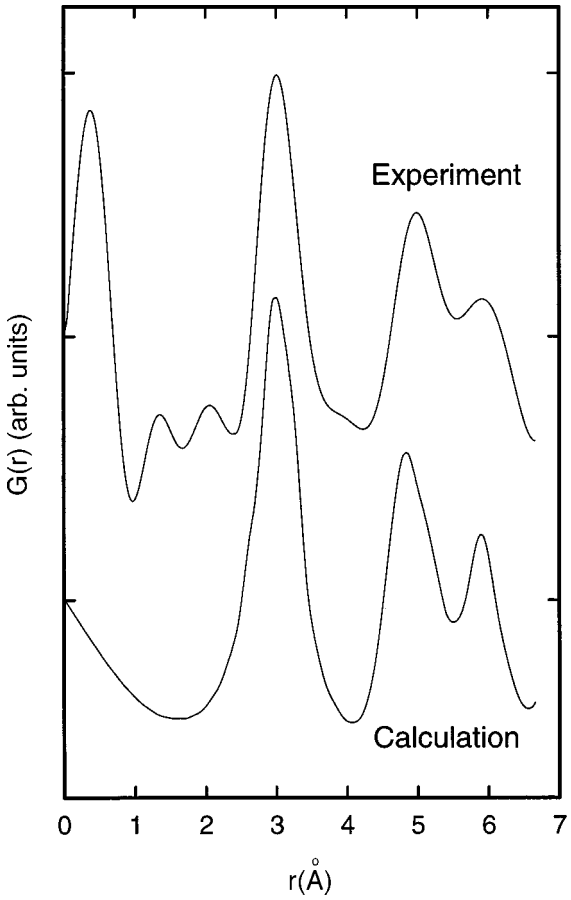

FIG. 11. Comparison of the calculated $G(r)$ for the *a*-W model with the experimental data.

diameter of a W atom is 2.52 Å. Therefore, these two models can be excluded. On the basis of the above considerations, three possible models for the A15 structure can be proposed: (i) an ordered W_3W structure (S0), i.e., normal ABCBABCB stacking; (ii) a stacking faulted ABABABAB structure (S1), and (iii) a 50% mixture of both S0 and S1 models (S0+S1).

Figure 10 shows a comparison between each theoretically calculated model and the experimental $G(r)$ in the range of 2.0–7.5 Å for the ordered crystalline A15 W sample. The experimental $G(r)$ shows a broader first peak centered at 2.96 Å, due to the existence of three peaks corresponding to the first, second, and third nearest neighbors ($r_1=2.52$, $r_2=2.82$, and $r_3=3.08$ Å, respectively). The second small peak at 3.80 Å is attributed to the existence of ordered substitutional or interstitial lattice defects in the A15 W structure. The peaks at higher r values correspond to higher-order neighbor atomic distributions. The calculated $G(r)$ for the S0 model has almost the same peak positions, shape, and amplitudes of the experimental observed peaks, however, it fails to predict the peak at 3.80 Å. The S1 model provides a feature at 3.84 Å, however, its amplitude is higher. In addition, for the S1 model the first peak is broader and the third peak splits into two peaks, in contrast to the experimental observations. The (S0+S1) model provides the best fit to all of the features, which is a good reproduction of the experimental $G(r)$. The relative percentages of S0 and S1 structures were not varied. This is direct evidence of the presence of mixed ordered and stacking faulted W_3W structures with approximately equal abundance. This mixed model of ordered and stacking faulted W_3W structures has been further confirmed by using the R factor analysis[30] to compare the experimental and calculated $G(r)$. It should be pointed out that differences between the (S0+S1) model and experiment can be clearly seen. The third peak at 4.74 Å from the calculated (S0+S1) model has a small shoulder at 5.19 Å and the fifth peak at substantially lower value (~6.96 Å) than the experimental one (~7.14 Å). We explain that such a discrepancy is related to stacking faults and localized disorder in the grain boundaries, leading to deviation from the perfect structure.

Figure 11 shows the experimentally measured $G(r)$ for the *a*-W structure. In the first two coordination shells, the first and second nearest-neighbor distances appear at about 3.02 and 4.98 Å, respectively. This is mainly due to a broad range of W–W (also W–O) next-neighbor distance in the less ordered specimen. The atomic distance observed becomes less localized, indicating the transition from a crystalline to an amorphous state. Features in the low-r region are the least reliable because they are most strongly affected by the small-angle inelastic scattering effect associated with a considerable fraction of small voids. Our XPS data show the presence of ~18 at. % oxygen in the *a*-W film, while the

EELS indicates 18–26 at. % oxygen. Therefore, the existence of a disordered tungsten suboxide W_3O is highly probable. Actually no general structural model exists, which permits us to describe the amorphous state. One way to represent the atomic arrangement of this state is the dense random packing (DRP) of the hard spheres model.[31] This model has been successfully used to produce the experimental $G(r)$ distributions for the a-WO_3 model in our previous study.[32] In this study, the amorphous model is a disordered phase of W_3O with A15 structural symmetries, consisting of a random continuous matrix. As one can see from Fig. 11, the calculated $G(r)$ compares quite well with the experimental data apart from some discrepancy in the second peak. The agreement of the first peak position between theory and experiment is very good, indicating that the first coordination shell is located at the mean bond length. However, in the second peak region the theory shows some differences between the model and the experimental data. The calculated second peak at ~4.84 Å is lower than the experimental one at ~4.98 Å. We believe that the discrepancy is related to inhomogeneities in real amorphous films, particularly voids on a scale of 50–100 Å.

IV. DISCUSSION

A. Kinetics of film growth and correlation between stress and microstructure

The kinetics of growth is controlled by the mobility of the atoms on the surface. This mobility can be enhanced by increasing the temperature or by supplying impact energy through ion bombardment. Since the experiments were performed as a function of sputtering-gas pressure at low temperatures with constant input power, we will consider only the effects of sputtering-gas pressure.

It is apparent from the above results that the dominant processes in sputter deposition, which control the kinetics and mechanisms during film growth, are changing at different sputtering-gas pressures. Monte Carlo (MC) calculations of such transport of sputtered atoms have been extremely helpful in delineating these processes. Under the present experimental conditions, a MC calculation[33] by one of the current authors indicates that Ar sputtering pressure determines the average impact energy of the sputtered W particles, as they arrive on the substrate. For example, the average impact energy of W changes from ~20.0 eV at 2 mTorr, 4.0 eV at 26 mTorr to 1.2 eV at 60 mTorr. The decrease in average impact energy with sputtering pressure is due to the increasing proportion of thermalized atoms and decreasing proportion of high energy atoms arriving at the substrate. For deposition at low pressures of 2–12 mTorr (corresponding to high impact energies in the range of 8–20 eV), penetration, local atomic rearrangements, and atomic displacements increase, and the original W particles as well as W atoms neighboring the collision site can acquire sufficient energy for mobility enhancement. When this enhancement is sufficient to overcome the surface diffusion barrier,[33] the atoms are able to reach sites, which are conducive to the stable crystalline growth. As the pressure increases, the mobility of W particles decreases. In addition, the incorporation of oxygen impurities in the films is significant at higher pressures, resulting in the formation of a metastable crystalline structure at intermediate pressures of 26 mTorr. The exact mechanism for the formation of the metastable phase stabilized by oxygen impurities is not clear. Further study with *ab initio* total-energy calculations for establishing the origin of the A15 W phase induced by a small amount of oxygen is in progress in our Materials Research Center. At a high pressure of ~60 mTorr, atomic displacements, local atomic rearrangements, and enhancement of mobilities are minimal. The W particles may not be sufficiently mobile to migrate to the preferred sites for the crystalline growth. This results in the accumulation of permanent defects, followed by transition to amorphous at larger thicknesses.

The stress and microstructure of the films are influenced by changing sputtering-gas pressure through ion bombardment. We have shown that the residual stress is an important parameter which either correlates with, or directly influences, most of the structural properties of W films deposited by dc magnetron sputtering. The features observed in the plots of Figs. 1, 2, and 4 are a manifestation of the correlation of the stress and microstructure. At low pressures the films contain a dense microstructure, without any columns, which is responsible for the observed compressive stress. Usually, the occurrence of residual stress is due to the atomic peening effect[24] caused by energetic particles such as sputtered atoms and sputtering-gas atoms or ions, leading to densification of the microstructure. The sputtered atoms normally arrive at the surface of the growing film with enhanced energy. These energetic particles strike the surface, limiting the development of a columnar growth morphology. With increasing Ar pressures, the films obtained show a columnar microstructure and develop a tensile stress. The columnar structure observed for the tensile stress films indicates the presence of voids in the material. This type of defect tends to shrink the films due to the high surface tension of the inner surface of the voids. As a result, the film volume decreases and tensile stress is generated. The films deposited at high pressures show a dendritic-like microstructure. It is evident that open columnar structures are unable to support large internal stress in the film.

B. The role of oxygen in forming and stabilizing the A15 W structure

During film growth oxygen is always incorporated in the films. The XPS results show that the bcc W, A15 W, and a-W films contained 1–2, 5–12, and 18 at. % oxygen (Fig. 6), while the EELS analysis indicates 1–4, 6–15, and 18–26 at. % oxygen (Fig. 7), respectively. These values were obtained based on repeated measurements involving many freshly deposited samples over many weeks. The good agreement between the oxygen impurities obtained from two independent techniques lends confidence to the oxygen concentration value and the reliability of the experimental data. The oxygen content became slightly less for higher film thickness.

In examining the W related phase diagram we have not been able to identify a unique bulk phase which could fully account for the observed A15 W structure. In light of this,

we envision that the A15 W phase is not characteristic of any bulk compound and therefore seems to be uniquely associated with the presence of incorporated oxygen. The fact that the A15 W phase appears over such a broad range of Ar sputtering pressures may be due to the fact that it is kinetically prevented from converting to thermodynamically favorable phase, bcc W, or that a very dilute bulk oxygen composition might be sufficient to completely stabilize the A15 W structure.

It is of interest to determine the thermal range of stability of the A15 W structure. It was found that a short anneal for several minutes at 625 °C was sufficient to complete the phase transformation from A15 W to bcc W (Fig. 8). The conclusion from the data is that annealing to temperatures of 625 °C (about $0.2T_m$, where T_m is the melting temperature of the bulk film) is sufficient to activate atom diffusion, atom exchange, and structure conversion. We conclude that thermally induced phase transformation may serve to stabilize the stable bcc structure, although the dynamics of the structure transformation are not known in detail. Above the temperatures of the activated transformation, the bcc W structures are stable to temperatures as high as $0.27-0.3T_m$ as long as this temperature is below about 850 °C, where reaction between the W film and Si substrate begins to occur at a significant rate.

Our combined EELS, TED, and XRD results indicate that by anneal the A15 W does not fully transform to the bcc W as long as the oxygen content remains above about 5 at. %. Only after a critical amount of oxygen in the film has been reduced, does the subsequent transformation of the structure occur. In other words, if the loss of oxygen in the film is locally increased above a certain level, then a transformation of the A15 W into the bcc W occurs. This can be explained in terms of original oxygen enrichment at the column boundaries in the A15 W film. With increasing temperature the oxygen atoms move increasingly outward. The pyrophoric nature of A15 W is an indication of how strongly oxygen can absorb on its surface. Based on the results obtained and the above discussion, the phase transformation from A15 W to bcc W in the film is believed to be governed by two main trends: (1) From an energetic point of view, the stacking faulted energy required to stabilize the A15 W structure must be overcome in order for transformation to occur. (2) From a structural point of view, the transformation to bcc W occurs by dissolution of the stacking faults and localized rearrangement of the lattice. No long-range diffusion or atomic movement is required.

C. Film structure

The results of the present investigation have shown that energy-filtered electron diffraction with reduced radial distribution function $G(r)$ analysis is a powerful technique, which is capable of detecting the structure of polycrystalline and amorphous thin films, and producing quantitative data of the atomic distance parameters. By comparing the experimental $G(r)$ with the model calculations, the structures of both the A15 W and *a*-W phases at the atomic level have been determined.

TED images reported by many research groups[7,15–17] reveal that the A15 W phase is not a perfect A15 structure because kinematically forbidden reflections are observed [also see Fig. 9(b)]. However, its exact structure remains unknown due to large uncertainties involved in diffraction and spectroscopic measurements. In this study the particular model was chosen because its simulated $G(r)$ scan [Fig. 10, curve (S0+S1)] provides better agreement with the experimental $G(r)$ scan (Fig. 10, experiment) than any other model. Good correspondence between the observed and calculated $G(r)$ distributions indicates that the A15 W is composed of ordered and stacking faulted W_3W structures.

Because of the small content of oxygen (about 5–12 at. % by XPS and 6–15 at. % by EELS) observed in the A15 films as well as its very small scattering power compared to tungsten, oxygen was not observed directly in the experimental $G(r)$ curves. However, it may have effects on the arrangements of heavier tungsten atom bonded to lighter oxygen. The effects on the bond distances are expected to be negligible, but the peak heights may be affected owing to the variations in W–W, O–O, and W–O coordination. We are currently examining this effect and related experiments.

Both XPS and EELS show that the *a*-W contains oxygen close to the 25 at. % oxygen necessary for a disordered W_3O stoichiometry. Therefore, the existence of a disordered tungsten suboxide is highly probable. The structure of an amorphous film is characterized by its local atomic ordering. It was frequently observed that this short-range atomic order exhibits similarities to the local symmetry of the corresponding crystalline compound. Overall, the $G(r)$ calculated based on the DRP model shows good agreement with the experimental data, although there are some regions of discrepancy. We believe that the discrepancy is related to inhomogeneties in real *a*-W films, particularly voids on a scale of 50–100 Å.

V. CONCLUSIONS

The stress and structural properties of the tungsten thin films prepared by dc magnetron sputtering have been studied at Ar sputtering pressures in the range of 2–100 mTorr. The film stress, determined *in situ* using a cantilever beam technique during the film formation, is found to strongly depend on the Ar pressure and changes from highly compressive to highly tensile in a relatively narrow range of 12–26 mTorr. The microstructures of these films were characterized using XRD and cross-sectional TEM. A strong correlation of the stress with the microstructure in the films is clarified. The results indicate that the compressively stressed films consist of single-phase bcc W or a mixture of bcc W and A15 W, while the films having the tensile stress have only A15 W structure. With elevated sputtering pressures between 60 and 100 mTorr, an amorphous tungsten is observed, resulting in complete relaxation of internal tensile stresses.

The role of oxygen impurities in the formation and stability of the A15 W structure was elucidated herein by XPS, EELS, TED, and XRD. Both XPS and EELS indicate that the A15 W structure is stabilized by a small amount of oxygen without forming an ordered W_3O compound. The thermal range of stability of the A15 phase was investigated by

in situ anneal in the TEM and EELS system. It is found that phase transformation from A15 W to bcc W by higher temperature annealing is accompanied by reduction of oxygen in the film. We believe that the reaction is controlled by a diffusive process at void surfaces and/or grain boundaries in the A15 phase.

The structures of the A15 W and *a*-W films formed at different sputtering-gas pressures were experimentally determined for the first time using energy-filtered electron diffraction with reduced radial distribution function $G(r)$ analysis. By comparing the experimental $G(r)$ with the theoretically calculated models, we propose that the A15 W crystal structure is composed of an ordered and stacking faulted W_3W compound, while the *a*-W phase is formed of a random continuous matrix of clusters with the W_3O-like symmetry.

ACKNOWLEDGMENT

The authors gratefully acknowledge the financial support of this project by the Australian Research Council. The authors also appreciate the use of the facilities in the Australian Key Center for Microscopy and Microanalysis, University of Sydney, which is supported by Australia Research Council.

[1] J. H. Souk, J. F. O'Hanlon, and J. Angillelo, J. Vac. Sci. Technol. A **3**, 2289 (1985).
[2] A. J. Learn and D. W. Foster, J. Appl. Phys. **58**, 2001 (1985).
[3] E. K. Broadbent, J. Vac. Sci. Technol. B **5**, 1661 (1987).
[4] Y. Pauleau, Ph. Lami, A. Tissier, R. Pantel, and J. C. Oberlin, Thin Solid Films **143**, 259 (1986).
[5] A. Bensaoula, J. C. Wolfe, A. Ignatiev, F. O. Fond, and T. S. Leung, J. Vac. Sci. Technol. A **2**, 389 (1984).
[6] A. M. Haghiri-Gosnet, F. R. Ladan, C. Mayeux, and H. Launois, Appl. Surf. Sci. **38**, 295 (1989); J. Vac. Sci. Technol. A **7**, 2663 (1989).
[7] P. Petroff, T. T. Sheng, A. K. Sinha, G. A. Rozgonyi, and F. B. Alexander, J. Appl. Phys. **44**, 2545 (1973).
[8] H. S. Witham, P. Chindandom, I. An, R. W. Collins, R. Messier, and K. Vedam, J. Vac. Sci. Technol. A **11**, 1881 (1993).
[9] S. Basavaiah and S. R. Pollack, J. Appl. Phys. **39**, 5548 (1968).
[10] N. Susa, S. Ando, and S. Adachi, J. Electrochem. Soc. **132**, 2245 (1985).
[11] M. S. Aouadi, R. R. Parsons, P. C. Wong, and K. A. R. Mitchell, J. Vac. Sci. Technol. A **10**, 273 (1992).
[12] M. Arita and I. Nishida, Jpn. J. Appl. Phys., Part 1 **32**, 1759 (1993).
[13] I. A. Weerasekera, S. I. Shah, D. V. Baxter, and K. M. Unruh, Appl. Phys. Lett. **64**, 3231 (1994).
[14] N. C. Anqastiniotis and B. H. Kear, Mater. Sci. Forum **79**, 357 (1995), and references therein.
[15] M. J. O'Keefe, J. T. Grant, and J. S. Solomon, J. Electron. Mater. **24**, 961 (1995).
[16] D. P. Basile, C. L. Bauer, S. Mahajan, A. G. Milnes, T. N. Jackson, and J. Degelormo, Mater. Sci. Eng., B **10**, 171 (1991).
[17] M. Arita and I. Nishida, Surf. Rev. Lett. **3**, 1191 (1996).
[18] F. J. Von Preissig, J. Appl. Phys. **66**, 4262 (1989).
[19] G. C. Stoney, Proc. R. Soc. London, Ser. A **32**, 172 (1909).
[20] D. R. McKenzie, D. A. Muller, and B. A. Pailthorpe, Phys. Rev. Lett. **67**, 773 (1991).
[21] D. J. H. Cockayne and D. R. McKenzie, Acta Crystallogr. **44**, 870 (1988).
[22] *International Tables for Crystallography*, Volume C, edited by A. J. C. Wilson (Kluwer Academic, The Netherlands, 1995).
[23] I. C. Noyan and J. B. Cohen, *Residual Stress; Measurement by Diffraction and Interpretation* (Springer, New York, 1987).
[24] J. A. Thornton and D. W. Hoffman, Thin Solid Films **171**, 5 (1989).
[25] Ph. Gouy-Pailler and Y. Pauleau, J. Vac. Sci. Technol. A **11**, 96 (1993).
[26] M. A. El Khakani, M. Chaker, and B. Le Drogoff, J. Vac. Sci. Technol. A **16**, 885 (1998).
[27] *ASM Metals Reference Book*, edited by M. Bauccio (American Society for Metals, Metals Park, OH, 1994).
[28] R. F. Egerton, *Electron Energy Loss Spectroscopy in the Electron Microscope*, 2nd ed. (Plenum, New York, 1996).
[29] A. K. Sinha, Prog. Mater. Sci. **15**, 79 (1973).
[30] Y. G. Shen, J. Yao, D. J. O'Connor, B. V. King, and R. J. MacDonald, Phys. Rev. B **56**, 9894 (1997); Y. G. Shen, A. Qayyum, O'Connor, and B. V. King, *ibid.* **58**, 10025 (1998).
[31] J. D. Bernal, Nature (London) **185**, 68 (1960); Proc. R. Soc. London, Ser. A **280**, 299 (1964).
[32] D. C. Green, PhD thesis, University of Sydney, 1991.
[33] G. M. Turner, I. S. Falconer, B. W. James, and D. R. McKenzie, J. Vac. Sci. Technol. A **10**, 455 (1992).